Multimodal high-resolution retinal imaging using a camera-based DMD-integrated adaptive optics flood-illumination ophthalmoscope

Léa Krafft, Pierre Senée, Elena Gofas, Olivier Thouvenin, Michael Atlan, Michel Paques, Serge Meimon, Pedro Mecê

Multimodal high-resolution retinal imaging using camera-based DMD-integrated Adaptive Optics Flood-Illumination Ophthalmoscope

LÉA KRAFFT[1,2], PIERRE SENÉE[1,2], ELENA GOFAS[2], OLIVIER THOUVENIN[3], MICHAEL ATLAN[2,3], MICHEL PAQUES[2], SERGE MEIMON[1,2,3,+], AND PEDRO MECÊ[2,3,+,*]

[1] DOTA, ONERA, Université Paris Saclay F-91123 Palaiseau, France
[2] Paris Eye Imaging Group, Centre d'Investigation Clinique 1423, Quinze-Vingts National Ophthalmology Hospital, DGOS, INSERM, Paris, France
[3] Institut Langevin, ESPCI Paris, CNRS, PSL University, Paris, France
[+] These authors equally contributed to this work
[*] pedro.mece@espci.fr

Compiled June 28, 2023

We demonstrate the feasibility of a multimodal adaptive optics flood-illumination ophthalmoscope, able to provide both bright-field and dark-field images (such as phase contrast). The multimodality was made possible by integrating a DMD at the illumination path to project a sequence of complementary high-resolution patterns into the retina. Through a versatile post-processing method that digitally selects backscattered or multiply-scattered photons, we were able: 1) to achieve up to 4-fold contrast increase of bright-field images when imaging the photoreceptor mosaic and nerve fibers, and 2) to visualize translucent retinal features such as capillaries, red blood cells, vessel walls, ganglion cells and photoreceptor inner segments through phase contrast.

http://dx.doi.org/10.1364/ao.XX.XXXXXX

The adaptive optics scanning laser ophthalmoscope (AO-SLO) [1] has become the primary technique to achieve *in-vivo* cellular resolution retinal imaging. In bright-field mode, highly contrasted images from photoreceptors (PR) and nerve fiber layer (NFL) can be obtained owing to the use of a confocal pinhole, filtering out multiply-scattered photons and detecting backscattered photons [1]. Additionally, the lateral displacement of the detection position compared to the illumination in AO-SLO made possible off-axis detection schemes revealing translucent retinal structures such as PR inner segment, red blood cell, vessel walls, capillaries and ganglion cells [2–4]. Such dark-field techniques explore multiple scattering and forward scattering photons to generate contrast from phase gradient [2, 5].

Although AO-SLO has proven its value, it is prone to image distortion due to its slow scanning speed relative to eye motion [6]. Reducing the image field-of-view (FOV) is a common strategy to mitigate intra-frame distortion. However, the typical image rate is still slow to track dynamic processes in the retina such as blood flow in capillaries. Conversely, camera-based adaptive optics flood illumination ophthalmoscope (AO-FIO) systems have demonstrated immunity to motion-induced artifacts across the FOV owing to their high throughput [7]. Nevertheless, AO-FIO has not been favored over AO-SLO because of its lack of confocal gating, deteriorating the image contrast in bright-field mode. Moreover, dark-field techniques have not been so far fully explored and demonstrated in AO-FIO, apart from preliminary results restricted to obtain such contrast in a narrow portion of the FOV [8, 9], consequently most of the translucent retinal features seen in AO-SLO are still not visible in AO-FIO.

Recent works have demonstrated that spatial filtering could be implemented in AO-FIO to enhance the imaging contrast on bright-field mode while still benefiting from the distortion-free images [10, 11]. Those works build on the use of programmable pattern projections with a digital micromirror device (DMD). The patterns generated by the DMD partially illuminate the FOV, decreasing the total number of detected multiply-scattered photons [10]. Then, spatial filtering was possible by putting to zero value the camera pixels corresponding to non-illuminated areas. Finally, images acquired with complementary patterns were recombined to form a full-field image with enhanced contrast. Lee et al. reported up to 3-fold contrast improvement compared to conventional AO-FIO images at a frame rate of $250Hz$ [11]. However, all these works only focused on exploring backscattered photons coming from illuminated areas to generate bright-field photoreceptor mosaic imaging in a narrow FOV. Here, we demonstrate the capability of a DMD-integrated AO-FIO to not only generate large FOV contrast-enhanced bright-field images but also to reveal translucent retinal features, not yet visible in AO-FIO through phase and absorption contrasts.

The DMD-integrated AO-FIO platform was previously described in detail elsewhere [10]. High-resolution illumination patterns generated by the retina-conjugated DMD were projected on the retina after being pre-compensated for ocular aberrations by the deformable mirror (DM). Hence, the double pass on the DM allowed for diffraction-limit resolution for both illumination (for patterns projection) and imaging. Projected patterns consisted of binary images generated by custom-built Python software. We used the manufacturer software *EasyProj*

to upload patterns and control the DMD, enabling to project static patterns or a sequence of patterns.

To demonstrate the multimodal ability of the system, we designed two different sequences of patterns: one favoring a higher contrast for bright-field imaging (named “Pattern sequence 1”), and another to favor a better contrast in phase contrast imaging (named "Pattern sequence 2”). A schematic of the patterns can be found in Figs. 2(a) and 3(a). Patterns spacing was based on the observation described in Fig.1(a), while the width was empirically determined by experiment prior to image acquisition. Pattern sequence 1 consisted of periodic vertical lines with a width of $28\mu m$, and spaced by $252\mu m$ over 3.5^o FOV. To illuminate different areas of the retina, the pattern was successively shifted by $55\mu m$ at $30Hz$. For a full cycle of illumination, 4 patterns were needed. Pattern sequence 2 consisted of a single horizontal line with a width of $100\mu m$ over 3.5^o FOV. 24 patterns were generated, each one subsequently shifted by $50\mu m$.

Images were acquired on four healthy subjects. Written informed consent was obtained from all participants in accordance with institutional guidelines. The experimental procedures adhered to the tenets of the Declaration of Helsinki. The participants were seated in front of the system, while their head was stabilized with a forehead and chin rest. A fixation target was used to guide their line of sight during the imaging session. Eye drops were used for pupil dilation. The total irradiance for the imaging and AO light sources was respectively $1700\mu W$ and $2.8\mu W$, which is below the ocular safety limits stipulated by the International Organization for Standardization (ISO) standards for group 1 devices.

Before image acquisition, a calibration step consisted of matching the focal planes of the camera and the DMD by moving a translation stage where the camera was mounted. Then, a final step before starting image acquisition consisted of using the DM to place the camera/DMD focal plane at the retinal layer of interest. The camera acquired images of 2048x2048 pixels at $100Hz$ (10ms exposure, which is sufficient to avoid motion blur [12]), while the illumination field-of-view, without any pattern projection, was as large as $3.5^o \times 3.5^o$. Before acquiring images with Pattern sequences 1 and 2, an image sequence without any pattern (equivalent to a conventional AO-FIO image, and named here Full-Field illumination) composed of 100 frames was acquired and served as a reference for image processing. The DMD projected the sequence of patterns at 30 Hz and was not synchronized with the camera acquisition (see Visualization 1 for examples of image sequences using Patterns 1 and 2). Because of the lack of synchronization, one-third of raw images presented artifacts originated from the transient states of the DMD micromirrors and needed to be discarded. To illuminate the same retinal area at least 50 times, image acquisition consisted of 500 and 3000 frames for Pattern sequences 1 and 2 respectively, enabling the reconstruction of full-field images. Images were acquired using custom-made open-source Holovibes software, allowing to apply a high-pass filter to eliminate multiply-scattered haze in real-time [7]. This software was particularly convenient for fine positioning of the imaging plane and DMD patterns at the retinal layer of interest.

After the acquisition, each image sequence was processed as follows. First, the reference sequence (without any pattern) was averaged after registering them using a custom-built high-spatial frequency-based phase correlation algorithm adapted to noisy AO-FIO images [13]. Then, the reference averaged image was used as a global reference to register (i.e. align) patterned images using the same registration algorithm. To generate the different image contrasts, by selecting photons detected in and out of illumination zones, we converted the binary patterns generated for the DMD into masks at the camera plane. Image shifts previously measured to correct eye motion were also applied to the masks. Then, we used the masks to do digital filtering (putting pixels outside the zone of interest to zero value), enabling us to generate the following contrasts: 1) Near-confocal bright-field imaging (henceforth denominated as Partial-Field illumination [10]), 2) Absorption contrast, and 3) Phase contrast. Partial-Field imaging consisted of putting to zero value all the pixels outside the zone of illumination, favoring the detection of backscattered ballistic photons, in a similar manner as previous DMD-integrated AO-FIO works [10, 11] and confocal AO-SLO. To generate Absorption and Phase contrasts, we respectively summed and subtracted two "offset" images [4, 5] generated with the Partial-Field masks shifted into two different directions. For example, in the case of Pattern sequence 2, Offset images 1 and 2 were respectively generated by putting to zero all pixels except those at the top (for offset 1) or the bottom (for offset 2) part just outside the illumination zone for a given number of pixels, here 100 (see Fig. 3).

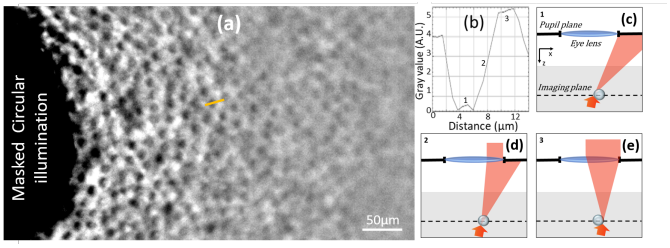

Fig. 1. (a) Cropped phase contrast image of PRs after masking the illumination area (black region). Note that the contrast start to decline for PRs located around 0.5^o away from the illuminated area. (b) Intensity profile across one photoreceptor (orange line) outlining the diphasic aspect. Labels 1-3 refers to the contrast mechanism described in (c-e), which is inspired by the model presented in [14].

Figure 1 highlights the ability of DMD-integrated AO-FIO to generate dark-field imaging. When projecting a static circular pattern, while focusing at the photoreceptor layer, a gradient contrast varying from dark to bright can be noticed in individual PRs located outside the illuminated zone. Such contrast is the hallmark of phase-gradient images seen in AO-SLO systems [5, 15]. In the case of AO-FIO, the principle can be explained as follows: multiply-scattered photons, originating from the illuminated area at a deeper layer, are refracted by a retinal feature, and filtered out by the eye’s pupil. The part of the retinal feature close to the illumination will refract light out of the eye’s pupil (Fig.1(c)) generating a dark contrast (label 1 in Fig.1(b)). On the other hand, the part of the retinal feature far from the illumination will refract light inside the eye’s pupil (Fig.1(e)), generating a bright contrast (label 3 in Fig. 1(c)). Such behavior has a strong similarity with oblique back-illumination microscopy [14]. Another interesting observation in Fig. 1(a) is that the further the photoreceptor is from the illuminated area, the lower the phase contrast. By taking advantage of these observations, we created two different pattern sequences to demonstrate the capability of DMD-integrated AO-FIO to achieve multimodal imaging, through post-processing selection of ballistic and multiply-scattered photons.

Figures 2 (a) and (b) present a comparison of images gener-

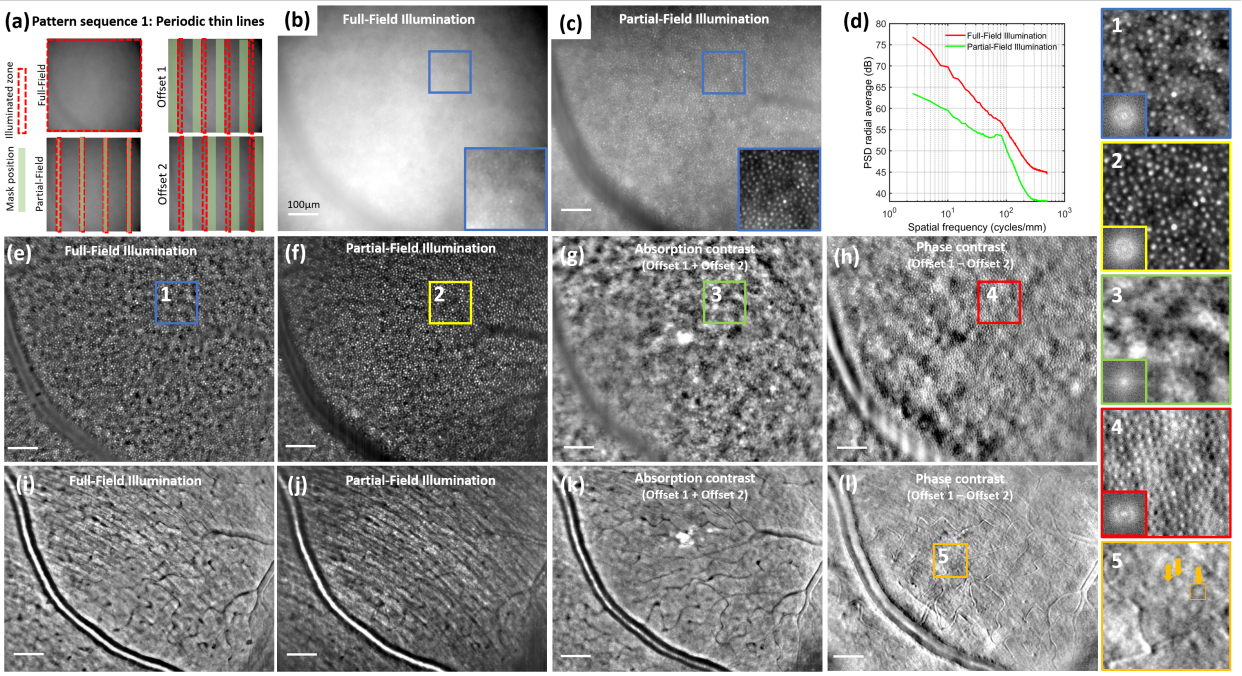

Fig. 2. (a) Pattern sequence 1 detection schemes. (b,c) Respectively Full-Field and Partial-Field images highlight the contrast gain. (d) Power spectral density from (b,c). (e,f) Respectively Full-Field and Partial-Field images after applying a digital high-pass filter. (g,h) Absorption and Phase contrast images of PRs respectively. (i-l) Respectively Full-field, Partial-Field, Absorption and Phase contrast for NFL imaging. (1-5) Magnified images and their respective Fourier Transform. Yellow arrows indicate ganglion cells and yellow box delineates a single one. Scale bar: $100\mu m$.

ated with Full-Field and Partial-Field illumination (see Fig. 2(c) for the detection schemes) at the same retinal eccentricity when imaging the photoreceptor layer (PRs). Thanks to the spatial filtering in Partial-Field image, the haze generated by the detection of multiply-scattered photons is decreased, hence the image presents a better contrast. We measured an averaged Michelson contrast of 6.6% and 26.6% for Full-Field and Partial-Field illumination respectively, for a 4-fold improvement. Further image improvement can be seen through the power spectral density of both images (Fig. 2(d)). Owing to the spatial filtering, not only the haze low-spatial frequency energy decreases, but the spectral signal-to-noise ratio increases from 17.1 to 37.6. These observations are in accordance with previous publications using DMD-based AO-FIO [10, 11]. Nevertheless, here, with our designed pattern, we were able to reconstruct an image with a larger field-of-view ($3.1^o \times 2.6^o$ against $0.7^o \times 0.7^o$), higher contrast gain (4 against 3) [11] and without any reconstruction artifacts [10]. In Full-Field illumination, it is common practice to filter out the multiply-scattered haze with digital filtering [7]. Even after digital filtering, it is possible to notice an improvement in Partial-Field images compared to Full-Field (Figs. 2 (e-f) and (i-j)). In both PRs and nerve fiber layer (NFL) imaging, better optical sectioning can be noticed. In the case of PRs imaging, optical sectioning leads to the disappearance of a medium-spatial frequency probably coming from out-of-focus choriocapillaris, and make vessel located posterior to PRs darker, as it is typically seen in high optical sectioning imaging systems, e.g. in AO-SLO [3] or in Full-Field OCT [16]. These changes also help to considerably increase photoreceptor mosaic contrast even after digital filtering. The increase of contrast is even more evident in the case of NFL imaging, where individual nerve fiber bundles become much more visible and contrasted, with the disappearance of capillary structures.

The same image sequence used to generate Partial-Field images can be processed to generate absorption and phase contrast images. To do so, we used the masks designed for Offset 1 and 2 (Fig. 2(c)). By summing Offset images 1 and 2, one can generate absorption contrast images of PRs and NFL (Figs. 2(g) and (k) respectively). For PRs, putative retinal pigment epithelium (RPE) [17] cells start to become visible, while PRs contrast decreases. In a similar manner, for NFL, nerve fibers disappear while previously rejected capillaries can be visualized. Finally, by subtracting Offset 1 from Offset 2, one can generate phase contrast images of PRs and NFL (Figs. 2(h) and (l) respectively). In this case, for PRs, photoreceptor mosaic is again visible, but with phase gradient contrast similar to the one obtained using split-detection AO-SLO [3, 5], which has been shown to correspond to the photoreceptor inner segment [3]. Now, for NFL, vessel and capillary walls have become highly contrasted, and putative ganglion cells (size: $10 - 12\mu m$) have started to be visible, in a similar manner and consistent size as it was previously shown for multi-offset AO-SLO [4, 5].

The thinner lines composing Pattern sequence 1 favor Partial-Field imaging to the detriment of Phase-contrast one. Indeed, with a thinner line fewer photons reach the retina, meaning that fewer photons will be multiply-scattered to contribute to the phase contrast. Moreover, using a periodic multi-line pattern with a short inter-line distance leads to a competition of opposite phase gradient (or cross-talk), decreasing or canceling out phase contrast. To favor phase contrast image, we designed and used Pattern sequence 2, composed of a single thicker line, increasing the number of photons being multiply-scattered, and avoiding contrast cross-talk. Figure 3 shows the results obtained with Full-Field (conventional AO-FIO), Partial-Field, and Phase contrast

imaging using Pattern sequence 2. For the Partial-Field case, the contrast presents a lower improvement compared to Pattern sequence 1 (2.9 against 4 for PRs case) and some PRs are not completely visible. On the other hand, phase contrast images of PRs and NFL are more contrasted. For PRs, we measured a Michelson contrast of 47% against 19% for Pattern sequence 1. Such an increase of contrast helps us to better appreciate the photoreceptor inner segment mosaic, where unseen PRs in bright-field mode can now be seen, as well as vessel walls, capillaries, individual fibers, and putative ganglion cells (size: $11\mu m$). One interesting fact about phase-contrast images is their directional dependence according to the illumination pattern. Indeed, one can see that the contrast gradient is oriented orthogonally to the direction of the line illumination (see PRs insets in Figs.2,3).

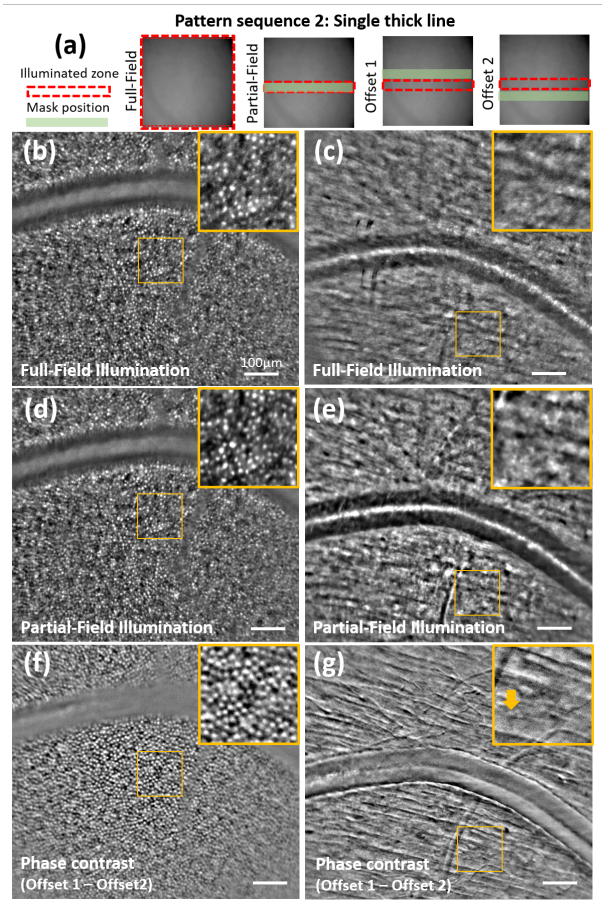

Fig. 3. (a) Pattern sequence 2 detection schemes. (b,c) Conventional AO-FIO images of PRs (b) and NFL (c). (d,e) Contrast-enhanced bright-field images of PRs (d) and NFL (e). (f,g) Phase contrast images of PRs (f) and NFL (g). Yellow arrow indicates ganglion cells. Scale bar: $100\mu m$.

One limitation of the presented system is the low effective frame rate, which is shown to be suitable to image static retinal features. However, to visualize retinal dynamic features, such as red blood cells, also commonly visualized in phase-contrast using AO-SLO [2], one can use static patterns and be again limited by the camera frame rate (see Visualizations 2 and 3). Another very interesting asset of the DMD-integrated AO-FIO is its versatility, as photons selection to generate all different contrasts can be done in post-processing. Such a tool can be helpful to design the most suitable masks to visualize a given retinal feature. Two examples of this versatility can be found in Visualizations 4 and 5. Visualization 4 shows that phase gradient contrast decreases as the detected areas are located further away from the illumination zone. This observation is in accordance with Fig. 1(a). Finally, the strategy presented here to generate multimodal images and enhance SNR bright-field imaging can also be applied to flood-illumination interferometric imaging techniques such as Full-Field OCT [16].

In this Letter, we proposed a DMD-integrated AO-FIO system able to generate multimodal retinal imaging, such as bright-field and dark-field (Absorption and Phase contrasts) images. The multimodal configuration was made possible by projecting a sequence of complementary patterns and by selecting in post-processing the image area where image reconstruction should take place. Owing to the given system, and the proposed acquisition/processing pipeline, we were able, at the same time, to: 1) obtain up to 4-fold contrast improvement in bright-field modality when imaging highly scattered structures such as PRs and NFL, and 2) to visualize, through phase contrast images, translucent retinal features such as capillaries, red blood cells, vessel walls, ganglion cells, and PRs inner segment.

Funding. Office National d'études et de Recherches Aérospatiales (PRF TELEMAC); Agence Nationale de la Recherche (ANR-18-IAHU-0001, ANR-22-CE19-0010-01).

Disclosures. The authors declare no conflicts of interest.

Data Availability Statement. All data is available upon request.

REFERENCES

1. A. Roorda, F. Romero-Borja, W. J. Donnelly III, H. Queener, T. J. Hebert, and M. C. Campbell, Opt. express **10**, 405 (2002).
2. T. Y. Chui, D. A. VanNasdale, and S. A. Burns, Biomed. optics express **3**, 2537 (2012).
3. P. Mecê, E. Gofas-Salas, M. Paques, K. Grieve, and S. Meimon, Biomed. optics express **11**, 4069 (2020).
4. E. Gofas-Salas, Y. Rui, P. Mecê, M. Zhang, V. C. Snyder, K. V. Vienola, D. M. Lee, J.-A. Sahel, K. Grieve, and E. A. Rossi, Biomed. Opt. Express **13**, 117 (2022).
5. P. Mecê, E. Gofas-Salas, Y. Rui, M. Zhang, J.-A. Sahel, and E. A. Rossi, Opt. letters **46**, 1085 (2021).
6. A. E. Salmon, R. F. Cooper, C. S. Langlo, A. Baghaie, A. Dubra, and J. Carroll, Transl. vision science & technology **6**, 9 (2017).
7. E. Gofas-Salas, P. Mecê, C. Petit, J. Jarosz, L. M. Mugnier, A. M. Bonnefois, K. Grieve, J. Sahel, M. Paques, and S. Meimon, Appl. Opt. **57**, 5635 (2018).
8. S. Meimon, E. G. Salas, P. Mecê, K. Grieve, J. A. Sahel, and M. Paques, Investig. Ophthalmol. & Vis. Sci. **59**, 4641 (2018).
9. E. Gofas-Salas, P. Mecê, L. Mugnier, A. M. Bonnefois, C. Petit, K. Grieve, J. Sahel, M. Paques, and S. Meimon, Biomed. optics express **10**, 2730 (2019).
10. L. Krafft, E. Gofas-Salas, Y. Lai-Tim, M. Paques, L. Mugnier, O. Thouvenin, P. Mecê, and S. Meimon, Appl. optics **60**, 9951 (2021).
11. S. Lee, S. S. Choi, R. K. Meleppat, R. J. Zawadzki, and N. Doble, Opt. Lett. **48**, 791 (2023).
12. J. Lu, B. Gu, X. Wang, and Y. Zhang, PloS one **12**, e0169358 (2017).
13. P. B. de Mecê, "4d exploration of the retina for adaptive optics-assisted laser photocoagulation," Ph.D. thesis, Université Sorbonne Paris Cité (2018).
14. T. N. Ford, K. K. Chu, and J. Mertz, Nat. Methods **9**, 1195 (2012).
15. A. Guevara-Torres, D. Williams, and J. Schallek, Opt. Lett. **45**, 840 (2020).
16. J. Scholler, K. Groux, K. Grieve, C. Boccara, and P. Mecê, Opt. Lett. **45**, 5901 (2020).
17. D. Scoles, Y. N. Sulai, and A. Dubra, Biomed. optics express **4**, 1710 (2013).

FULL REFERENCES

1. A. Roorda, F. Romero-Borja, W. J. Donnelly III, H. Queener, T. J. Hebert, and M. C. Campbell, "Adaptive optics scanning laser ophthalmoscopy," Opt. express **10**, 405–412 (2002).
2. T. Y. Chui, D. A. VanNasdale, and S. A. Burns, "The use of forward scatter to improve retinal vascular imaging with an adaptive optics scanning laser ophthalmoscope," Biomed. optics express **3**, 2537–2549 (2012).
3. P. Mecê, E. Gofas-Salas, M. Paques, K. Grieve, and S. Meimon, "Optical incoherence tomography: a method to generate tomographic retinal cross-sections with non-interferometric adaptive optics ophthalmoscopes," Biomed. optics express **11**, 4069–4084 (2020).
4. E. Gofas-Salas, Y. Rui, P. Mecê, M. Zhang, V. C. Snyder, K. V. Vienola, D. M. Lee, J.-A. Sahel, K. Grieve, and E. A. Rossi, "Design of a radial multi-offset detection pattern for in vivo phase contrast imaging of the inner retina in humans," Biomed. Opt. Express **13**, 117–132 (2022).
5. P. Mecê, E. Gofas-Salas, Y. Rui, M. Zhang, J.-A. Sahel, and E. A. Rossi, "Spatial-frequency-based image reconstruction to improve image contrast in multi-offset adaptive optics ophthalmoscopy," Opt. letters **46**, 1085–1088 (2021).
6. A. E. Salmon, R. F. Cooper, C. S. Langlo, A. Baghaie, A. Dubra, and J. Carroll, "An automated reference frame selection (arfs) algorithm for cone imaging with adaptive optics scanning light ophthalmoscopy," Transl. vision science & technology **6**, 9–9 (2017).
7. E. Gofas-Salas, P. Mecê, C. Petit, J. Jarosz, L. M. Mugnier, A. M. Bonnefois, K. Grieve, J. Sahel, M. Paques, and S. Meimon, "High loop rate adaptive optics flood illumination ophthalmoscope with structured illumination capability," Appl. Opt. **57**, 5635–5642 (2018).
8. S. Meimon, E. G. Salas, P. Mecê, K. Grieve, J. A. Sahel, and M. Paques, "Manipulation of the illumination geometry on adaptive optics (ao) flood illumination ophthalmoscope (fio) for dark field imaging of the retina," Investig. Ophthalmol. & Vis. Sci. **59**, 4641–4641 (2018).
9. E. Gofas-Salas, P. Mecê, L. Mugnier, A. M. Bonnefois, C. Petit, K. Grieve, J. Sahel, M. Paques, and S. Meimon, "Near infrared adaptive optics flood illumination retinal angiography," Biomed. optics express **10**, 2730–2743 (2019).
10. L. Krafft, E. Gofas-Salas, Y. Lai-Tim, M. Paques, L. Mugnier, O. Thouvenin, P. Mecê, and S. Meimon, "Partial-field illumination ophthalmoscope: improving the contrast of a camera-based retinal imager," Appl. optics **60**, 9951–9956 (2021).
11. S. Lee, S. S. Choi, R. K. Meleppat, R. J. Zawadzki, and N. Doble, "Programmable, high-speed, adaptive optics partially confocal multispot ophthalmoscope using a digital micromirror device," Opt. Lett. **48**, 791–794 (2023).
12. J. Lu, B. Gu, X. Wang, and Y. Zhang, "High-speed adaptive optics line scan confocal retinal imaging for human eye," PloS one **12**, e0169358 (2017).
13. P. B. de Mecê, "4d exploration of the retina for adaptive optics-assisted laser photocoagulation," Ph.D. thesis, Université Sorbonne Paris Cité (2018).
14. T. N. Ford, K. K. Chu, and J. Mertz, "Phase-gradient microscopy in thick tissue with oblique back-illumination," Nat. Methods **9**, 1195–1197 (2012).
15. A. Guevara-Torres, D. Williams, and J. Schallek, "Origin of cell contrast in offset aperture adaptive optics ophthalmoscopy," Opt. Lett. **45**, 840–843 (2020).
16. J. Scholler, K. Groux, K. Grieve, C. Boccara, and P. Mecê, "Adaptive-glasses time-domain ffoct for wide-field high-resolution retinal imaging with increased snr," Opt. Lett. **45**, 5901–5904 (2020).
17. D. Scoles, Y. N. Sulai, and A. Dubra, "In vivo dark-field imaging of the retinal pigment epithelium cell mosaic," Biomed. optics express **4**, 1710–1723 (2013).